Growth of wafer-scale graphene-hexagonal boron nitride vertical heterostructure with a clear interface for atomically thin electric analog
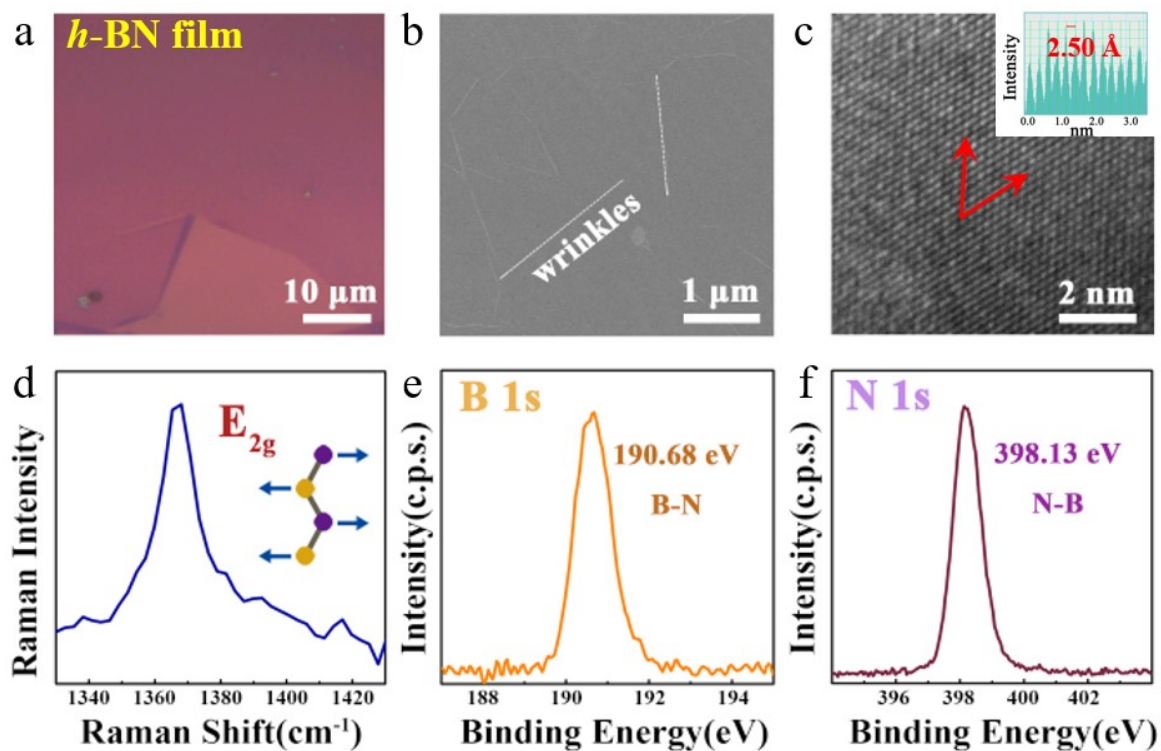
Figure S1 Characterization of the synthesized *h*-BN on Cu/Ni alloy. a) and b) OM and SEM images of the as-grown BN films. c) HRTEM image of the *h*-BN film, inset is the intensity profile. d) Raman spectrum of the *h*-BN film on Cu/Ni alloy substrates. XPS image of e) B 1s and f) N 1s peaks of the *h*-BN sample on SiO$_2$/Si.
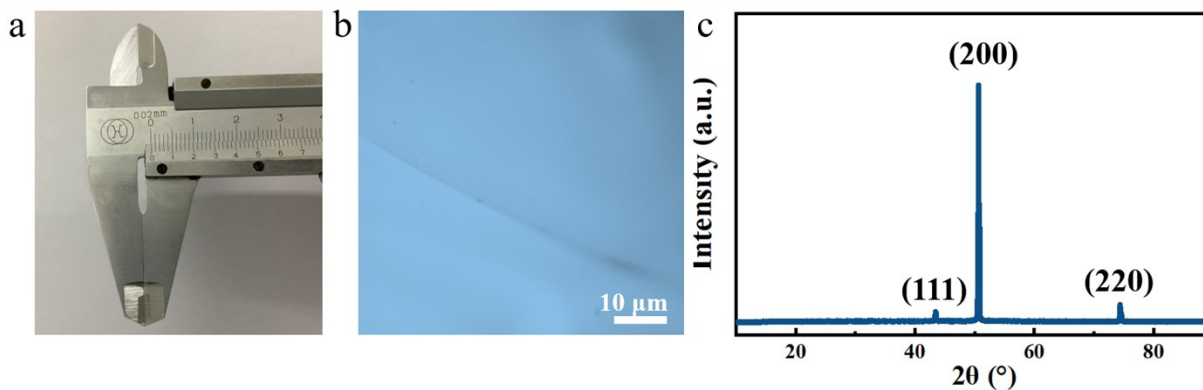
Figure S2 Characterization of the Cu/Ni alloy. a) $Cu_{0.8}Ni_{0.2}$ alloy foil with a thickness of around 25 μm. b) OM images of the $Cu_{0.8}Ni_{0.2}$ alloy after annealing treatment. c) XRD image of the $Cu_{0.8}Ni_{0.2}$ alloy.

The thickness of all the alloys adopted in our experiments are controlled to be around 25 μm (by coarse control on the area of the starting Cu and current density and time of the plating process, and then followed by fine control on the percentage of the Ni content by weighing with a mass balance and thickness by measuring). The Cu/Ni alloy after high-temperature annealing treatment demonstrates clear crystal boundaries in the optical micrograph in Fig. S2b. X-ray Diffraction(XRD) of the Cu/Ni alloy shows strong and sharp peaks around 43.45, 50.68, and 74.41 degrees, which corresponds to the lattice planes of (111), (200), (220).
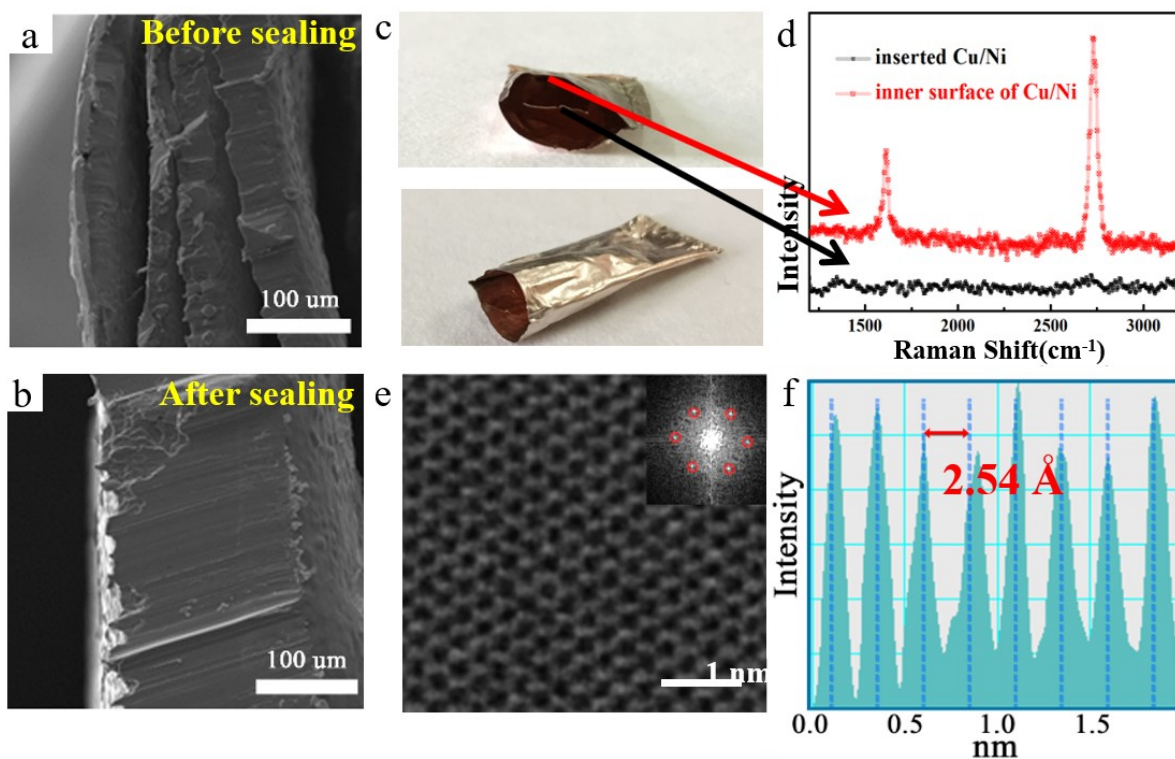
Figure S3 Characterization of the Cu/Ni alloy pocket and the synthesized graphene via diffusion method. a) and b) SEM images of the cross-section of the edges of the pockets before and after high-temperature sealing. c) Digital micrograph of the typical alloy enclosures cut in the middle from the front and side views. The same alloy foil is inserted into the pocket. d) Raman spectra of the as-grown graphene films on the inner surface of the alloy and the inserted alloy foil. e) HRTEM image of graphene, inset is the FFT image. f) Intensity profile of the line shown in c).

To check the impermeability of the alloy pocket, we characterize the cross-section of the edges. SEM images in Fig. S3b show that the alloy is fully fused into one integral layer without gaps. For comparison, the cross-section of the alloy pockets simply cramped but not annealed at high temperature shows 4-layer separate folds in Fig. S3a. These can verify that via tight cramping

and high temperature annealing, the edges can be completely integrated and the pocket is totally sealed.

Contrast experiments of the growth of graphene films via the metal-assisted method are performed. To fully testify the growth path to be diffusion instead of the surface-mediated growth, an alloy foil that is totally identical with the components of the pocket is inserted in the interior. After the complete growth process, both the samples acquired in the inner surface of the Cu/Ni alloy pocket and the inserted alloy foil are transferred and tested by a Raman spectroscope. The results are shown in Fig. S3 d. No feature peaks of graphene are observed from the sample obtained on the surface of the inserted alloy foil, which can fully verify the impermeability of the alloy enclosure and elucidate the possibility of a gaseous surface-mediated growth mechanism.
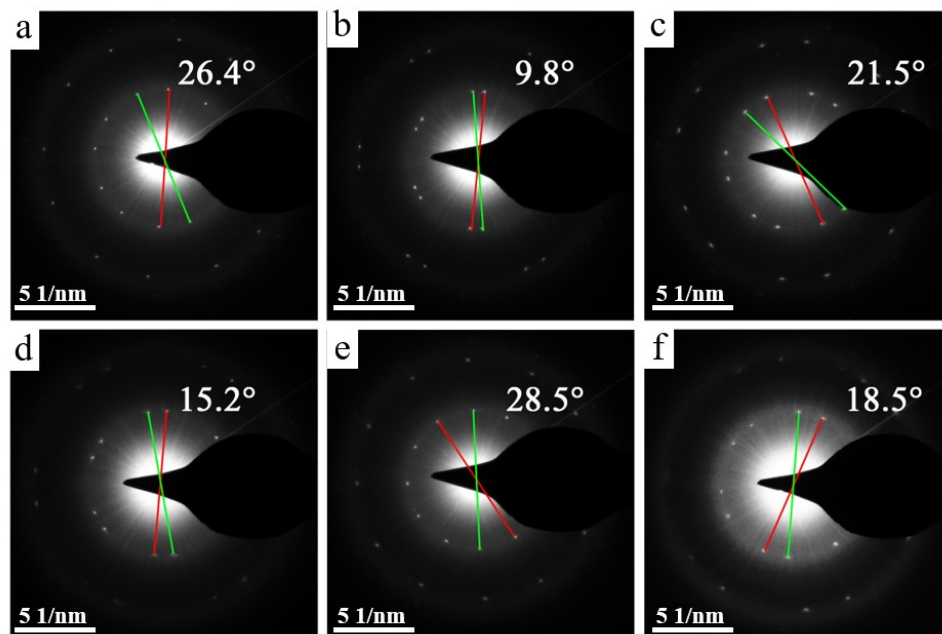
Figure S4 Characterization of lattice relation of the synthesized 1L *h*-BN/Gr heterostructure.

a) - f) SAED patterns obtained at different positions over a large region cross several millimeters

of the same *h*-BN/Gr vertical heterostructure, which demonstrates varied lattice orientations.
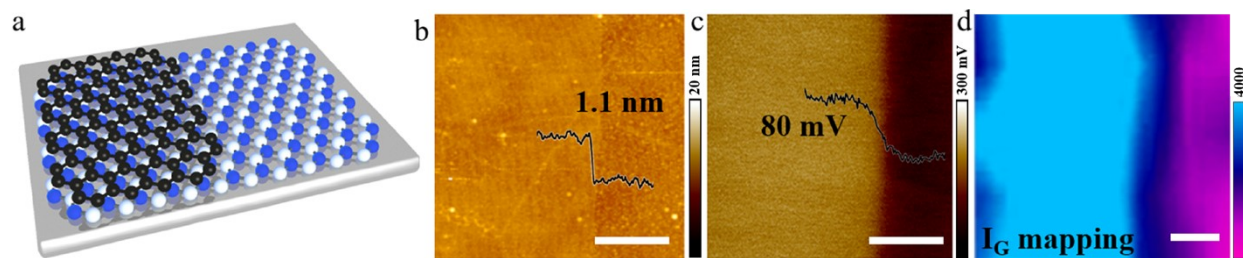
Figure S5 Characterization of the pattern with only half of the Gr layer lying on *h*-BN film.

a) Schematic image of the pattern with half of the Gr layer selectively etched. b) AFM image and

c) KPFM image of the structure. d) Raman mapping of I_G signal of the structure, the scale bar is 2

μm.
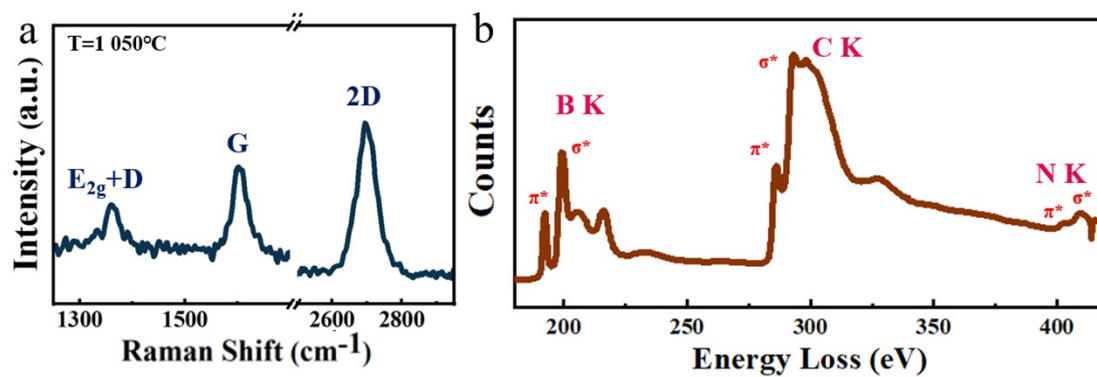
Figure S6 Characterization of the *h*-BN/Gr vertical heterostructure at a diffusion temperature of 1 050 ℃ on Cu$_{0.8}$Ni$_{0.2}$.
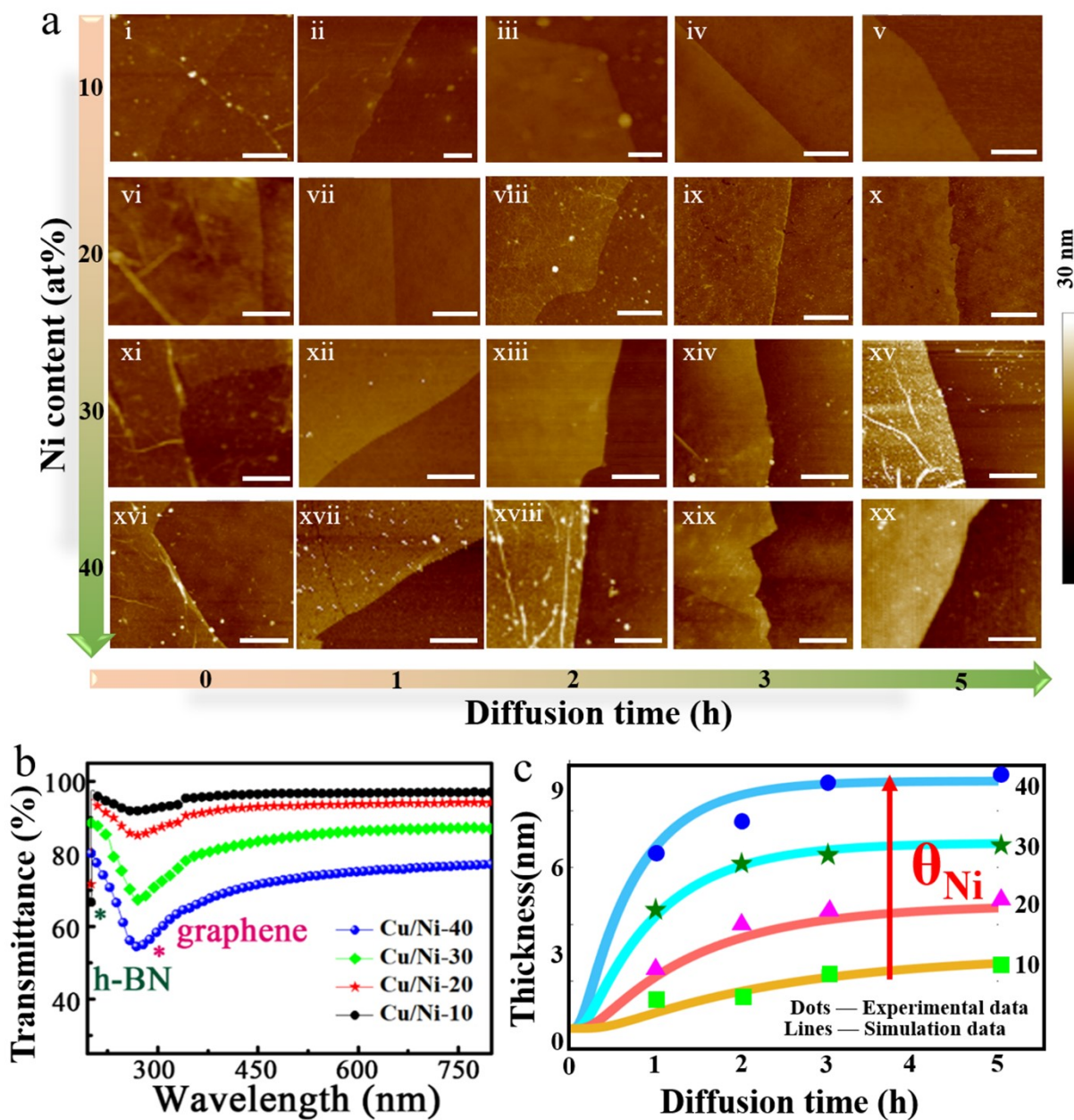
Figure S7 Characterizations of *h*-BN/Gr samples with increasing Ni content of the Cu/Ni alloy. a) AFM images of the heterostructure synthesized via increasing diffusion time and Ni content in the alloy. The scale bar is 200 nm in i-vii, 1 μm in viii-xii, and 5 μm in xiii-xx. b) UV-Vis absorption spectra of the *h*-BN/Gr heterostructures with different thicknesses obtained on

Cu/Ni alloys with increasing Ni content after 1 h diffusion. d) Thickness changes of the heterostructure over diffusion time and Ni content. The top layer *h*-BN is set to be about 1 layer by controlling the growing time. As the diffusion time and Ni content increase, the thickness of underlying graphene increases.

To explain this relationship, we perform a theoretical simulation on the diffusion process, the schematic illustration of the physical model is displayed in Fig. 3b. Assuming all the carbon atoms segregate at the inside interface form into graphene and the layer number(N) is only related with the total segregate flux (J), which are basically determined by the diffusion distance(x), diffusion time(t), and also the weight percent of Ni(n) in the alloy in our diffusion system. At time t, the segregate flux J_t at the location of x=L(L is the thickness of the alloy) can be can be expressed in the following equation:

$$J_t = \frac{\Delta m}{Sdt} = \frac{\Delta N_t k q_u m_c}{k S_u dt} = \frac{4\sqrt{3} m_c \Delta N_t}{9 a_c^2 dt} \qquad (S1)$$

where Δm is the mass of the carbon atoms diffused through the cross-sectional area(S) of the alloy per unit time(dt). ΔN_t is the layer number of newly formed graphene per unit time. k is the number of hexagon units per layer of graphene. q_u is the number of carbon atoms per hexagon unit in graphene. m_c is the atomic mass of each carbon atom. S_u is the area of one hexagon unit in graphene and a_c is the C-C bond length of graphene. Thus we can get the function expression of the layer number of the heterostructure with the segregate flux J_t:

$$N = N_G + N_{h\text{-}BN} = \sum_{t=0}^{t} \Delta N_t + 1 = \int_0^t \frac{3\sqrt{3} a_c^2 J_t}{4 m_c} + 1 \qquad (S2)$$

From Fick's first law, J_t is dependent on the solubility(C) gradient and diffusivity (D) of carbon atoms.

$$J_t = -D_n \frac{dC(n,L,t)}{dx} \tag{S3}$$

As the initial solubility and diffusivity of carbon atoms in Ni is far larger than that in Cu, we can presume that the values of them in alloys are linearly correlative with that in pure Ni for simplification and the correlation coefficient is the Ni content in the alloys:

$$D_n = nD_{Ni}, C_0 = nC_{Ni} \tag{S4}$$

According to the Fick's second law:

$$\frac{\partial C(n,x,t)}{\partial t} = -D_n \frac{\partial^2 C(n,x,t)}{\partial x^2} \tag{S5}$$

which conforms to the boundary conditions as follows:

$$t > 0, x = 0, C = C_0 \tag{S6}$$

$$t = 0, x \geq 0, C = 0 \tag{S7}$$

The total layer number of the heterostructure can be obtained via the integrating equation in (S2) when substitute different Ni contents. Systematical experiments are performed to figure out the relevance of the layer number graphene in the heterostructure over prolonged diffusion time through different alloys. The atomic content of Ni in the alloys is set to be 10 %, 20 %,30 %, and 40 %, while the diffusion time is set to be 1 h, 2 h, 3 h, and 5 h. The layer number is roughly defined by AFM measurements and the results are summed up in Fig. S7 c(dots). The theoretical result is also demonstrated here(lines).
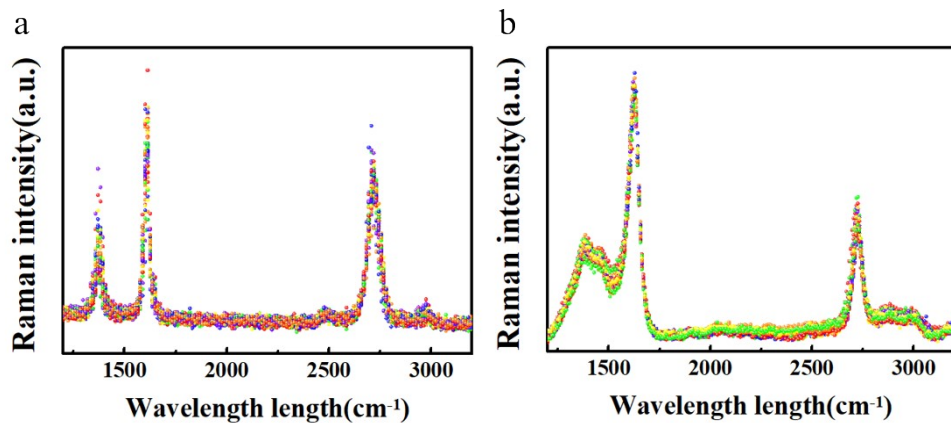
Figure S8 Uniformity of *h*-BN/Gr heterostructure with multi-layer graphene. a) and b) Raman spectra distributions of the *h*-BN/Gr heterostructure concluding ~3 layers and ~8 layers graphene, separately.
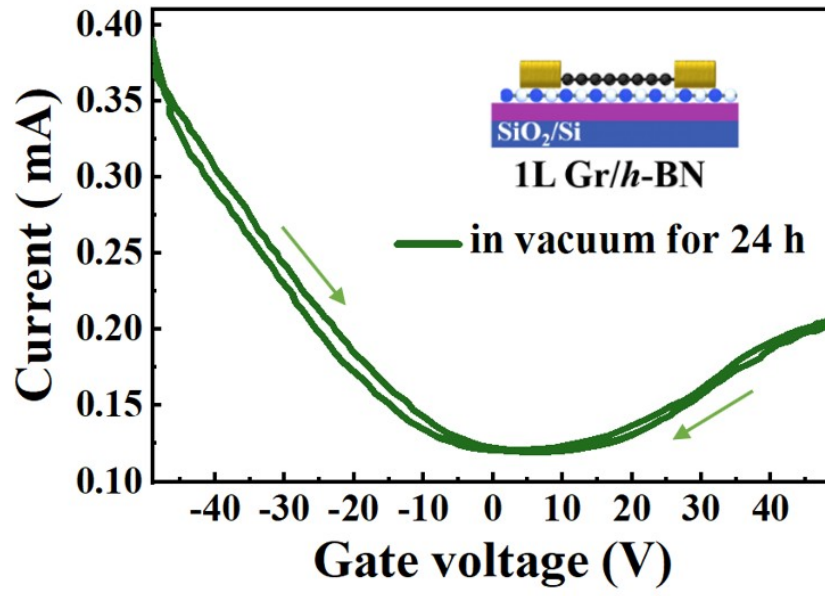
Figure S9 Hysteresis-free behavior of FET devices based on the *h*-BN/Gr heterostructure after long-time vacuum treatment.
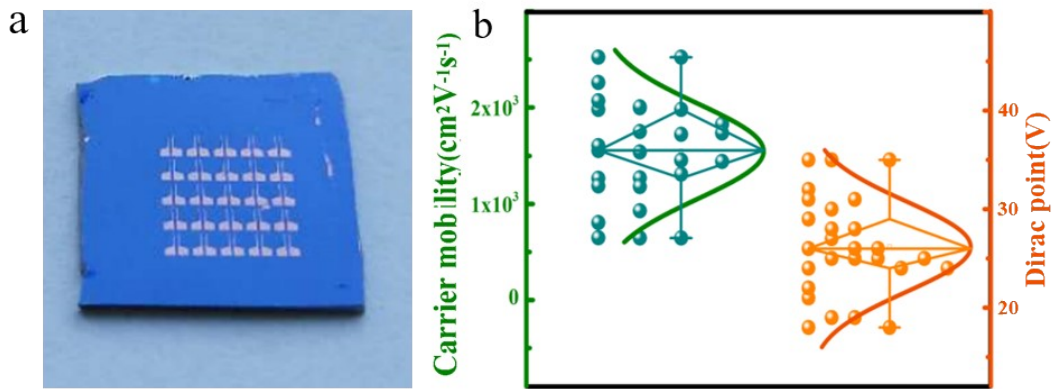
Figure S10 Electrical performance of the *h*-BN/Gr array devices. a) Digital image of the FET array of the *h*-BN/Gr heterostructures. b) Distributions of the carrier mobility and Dirac point of the devices in a, measured under room temperature and ambient atmosphere.
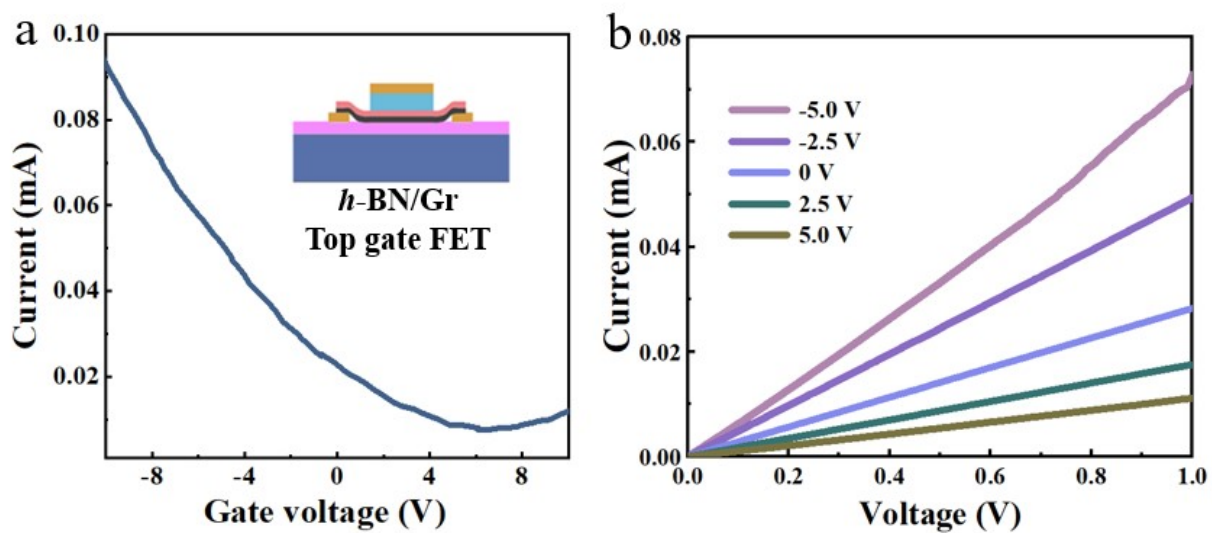
Figure S11 Device performance of the top-gate FET of *h*-BN/Gr heterostructure. a) transfer

curve and b) output curve of the FET device of the *h*-BN/Gr heterostructure.